Aggregation and mobility of membrane proteins interplay with local lipid order in the plasma membrane of T cells

Iztok Urbančič[1,2] (iD), Lisa Schiffelers[1] (iD), Edward Jenkins[1], Weijian Gong[1], Ana Mafalda Santos[1] (iD), Falk Schneider[1] (iD), Caitlin O'Brien-Ball[1] (iD), Mai Tuyet Vuong[1], Nicole Ashman[1] (iD), Erdinc Sezgin[1,3] (iD) and Christian Eggeling[1,4,5] (iD)

1 MRC Weatherall Institute of Molecular Medicine, University of Oxford, UK
2 Jožef Stefan Institute, Ljubljana, Slovenia
3 Science for Life Laboratory, Karolinska Institutet, Solna, Sweden
4 Institute of Applied Optics and Biophysics, Friedrich-Schiller-University Jena, Germany
5 Leibniz Institute of Photonic Technology e.V., Jena, Germany

Correspondence
I. Urbančič, E. Sezgin and C. Eggeling, MRC Weatherall Institute of Molecular Medicine, University of Oxford, Oxford, UK
Tel: +38 614773193
E-mail: iztok.urbancic@ijs.si (I.U.); erdinc.sezgin@ki.se (E.S.); christian.eggeling@uni-jena.de (C.E.)

To disentangle the elusive lipid–protein interactions in T-cell activation, we investigate how externally imposed variations in mobility of key membrane proteins (T-cell receptor [TCR], kinase Lck, and phosphatase CD45) affect the local lipid order and protein colocalisation. Using spectral imaging with polarity-sensitive membrane probes in model membranes and live Jurkat T cells, we find that partial immobilisation of proteins (including TCR) by aggregation or ligand binding changes their preference towards a more ordered lipid environment, which can recruit Lck. Our data suggest that the cellular membrane is poised to modulate the frequency of protein encounters upon alterations of their mobility, for example in ligand binding, which offers new mechanistic insight into the involvement of lipid-mediated interactions in membrane-hosted signalling events.

Cellular plasma-membrane hosts numerous vital processes, synchronously executed by a multitude of proteins, embedded in the fluid lipid bilayer. This mix of various lipid species and proteins is prone to segregate in more tightly or loosely packed patches, enriched by lipids with saturated or unsaturated alkyl chains and cholesterol, respectively, and differing in local lipid order, thickness, and molecular mobility [1, 2]. Employing model membrane systems that exhibit large-scale binary phase separation of lipids, often termed as liquid-ordered (Lo) and liquid-disordered phase (Ld), further investigations revealed that membrane proteins prefer one or the other type of environment based on the structural properties of their transmembrane domains, such as its length, surface area, and lipidation [3, 4]. Membrane proteins therefore remodel their local lipid environment accordingly, which can supposedly mediate protein–protein interactions, favouring encounters between proteins in patches of similar lipid composition, order, and thickness [5]. Nevertheless, it has been notoriously difficult to experimentally dissect this subtle interplay in

Abbreviations
BCR, B-cell receptors; DCA, deoxycholic acid; Fab, antigen-binding fragment; FCS, Fluorescence correlation spectroscopy; GPMVs, giant plasma-membrane vesicles; HBS, HEPES-buffered saline; ITAM, immunoreceptor tyrosine-based activation motifs; Ld, liquid-disordered phase; Lo, liquid-ordered phase; mNG, mNeonGreen; NEM, n-ethylmaleimide; Ni-NTA, nickel-nitrilotriacetic acid; pMHC, peptide-loaded major histocompatibility complex; SLB, supported lipid bilayer; SUVs, small unilamellar vesicles; TCR, T-cell receptor; tm, transmembrane domain.

protein reorganisation observed in trafficking and signalling [6, 7], for example, during activation of T lymphocytes [8–10].

Activation of T cells, a key element of our adaptive immune response, has been studied extensively to reveal the cellular machinery behind the recognition of foreign antigens [8]. The very first step in T-cell activation relies on spatiotemporal orchestration of a few key proteins on the plasma membrane: Upon binding of the ligand to the T-cell receptor (TCR), immunoreceptor tyrosine-based activation motifs (ITAM) on the TCR-CD3 complex are phosphorylated by a Src family tyrosine kinase (Lck), triggering the signalling cascade downstream. In a resting cell, activation is prevented by constant dephosphorylation of these ITAMs by the phosphatase CD45. To explain the shift in phosphorylation balance, required for activation, several models have been proposed. The kinetic-segregation model [11] advocates that the phosphatase CD45 is sterically excluded from the close contact zone with the antigen-presenting cell to elicit activation. Alternative models involve conformational change of the TCR upon binding ligands [12, 13] or cholesterol [14], and membrane compartmentalisation [15, 16].

While the exact mechanism for the triggering of the TCR remains unclear, mounting evidence has accumulated on the involvement of membrane heterogeneities in T-cell activation [7, 10]. However, the detailed roles of dynamic nanoscale membrane organisation in such processes have remained elusive [1, 2], primarily due to challenges to experimentally access the relevant spatiotemporal regimes. The first insights were provided by biochemical methods, such as the detergent resistance assay, indicating that upon T-cell activation, TCR is relocated from detergent-soluble to detergent-resistant membrane regions (more ordered due to high contents of cholesterol and saturated lipids), which also hosts Lck but not CD45 [17–19]. However, these invasive methods are notoriously sensitive to experimental conditions [2], casting doubt over reliability and relevance of such conclusions.

To complement these results with gentler experimental methods, several imaging-based approaches have been applied. By inducing ordered membrane patches large enough to be discernible with a conventional confocal microscope, these were found to colocalise with TCR and Lck, but not with CD45 [20, 21]. Similarly, antibody-induced patches of TCR coincided with higher lipid order, reported by spectral shifts of a polarity-sensitive membrane probe Laurdan [22], from which they concluded that TCR in resting cells prefers ordered lipid environment, contradicting the detergent solubility observations. Without such artificial

aggregation, conflicting associations of TCR with one or the other membrane environment have been reported in activated live T cells [23–27] using various advanced optical methods, such as Förster resonance energy transfer (FRET), fluorescence lifetime imaging, or super-resolution microscopy. These were likely difficult to reconcile due to different conditions employed (imaging live or fixed cells of different types, different resting/activating states [28]), and high TCR density in the nonaggregated state of resting T cells. To this end, model membranes had to be used, where the studies predominantly found monomeric TCR in the disordered membrane areas [29, 30].

Though the overview above indicates that TCR may change its preference for its membrane milieu from disordered in the resting state to more ordered in the activated state of the T cell, no mechanism has been provided to compellingly explain this switch in the partitioning behaviour. To elucidate this lipid–protein interplay, we investigated the lipid environment of TCR and other membrane proteins in giant plasma-membrane vesicles (GPMVs), the most physiologically relevant passive model membrane system, and live Jurkat T cells, using spectral imaging with polarity-sensitive membrane dyes and detailed spectral analysis. Focussing on the effects of protein aggregation and alterations to their mobility, we find that partial immobilisation of any tested membrane protein, including TCR, can locally elicit increased lipid ordering, which can enhance interactions with proteins that prefer such an environment, for example Lck. Though we cannot firmly conclude whether the observed effects participate in, or rather result from, the activation of a T cell, our insights nevertheless potentiate a general biophysical mechanism for reorganisation of local membrane order. This mechanism could also be applicable to related signalling pathways employing similar machinery, for example in the activation of B cells [31, 32] and mast cells [33, 34].

Results and Discussion

Partitioning of proteins in phase-separated GPMVs

We first investigated which lipid environment the proteins that take part in T-cell signalling (TCR, CD45, Lck, CD4, LAT, CTLA-4, and CD28 as well as its ligand CD86 from antigen-presenting cells) prefer based on their structural properties, such as hydrophobicity, length of the transmembrane domain, and lipidation [4]. To this end, we expressed their transmembrane domains (tm, and in the case of Lck

its membrane-anchoring SH4 domain), fused to a fluorescent protein, in HEK 293T cells, chosen for their high expression capabilities. Only the multispan protein complex TCR was expressed in Jurkat T cells to ensure proper membrane presentation. From these cells, we prepared GPMVs [35] containing the fluorescent membrane proteins. By cooling the vesicles to 4 °C and addition of deoxycholic acid (DCA), we induced large-scale separation of the vesicles' membrane into more ordered and disordered lipid regions, termed Lo and Ld phases, respectively [36], and verified the protein's colocalisation with the Ld phase marker Atto647N-PE [37] (Fig. 1A). From the intensity values of two-colour confocal images of the equatorial planes of GPMVs (Fig. S1), we further calculated the fraction of molecules partitioning into the Lo phase (Fig. 1B). While TCR and tmCD45

showed a similar preference for the disordered phase as the Ld marker (PE), Lck (SH4) showed a distinct preference for the ordered membrane environment (Fig. 1B).

Our data for Lck (SH4) agree with the published literature, where it has consistently been observed in the ordered lipid environment [38–40]. A similar preference for the ordered lipid environment was displayed also by transmembrane domains of CD4 and LAT (Fig. S2A), which are also closely involved in the activation of T cells. Given that partitioning to the Lo phase is most strongly driven by post-translational lipidation of the proteins [4], we next verified the roles of these fatty-acid modifications by repeating the experiments expressing Lck (SH4), tmCD4, and tmLAT with mutated cysteine residues, eliminating their palmitoylation sites (Fig. S2B–D). For CD4 with a single cysteine
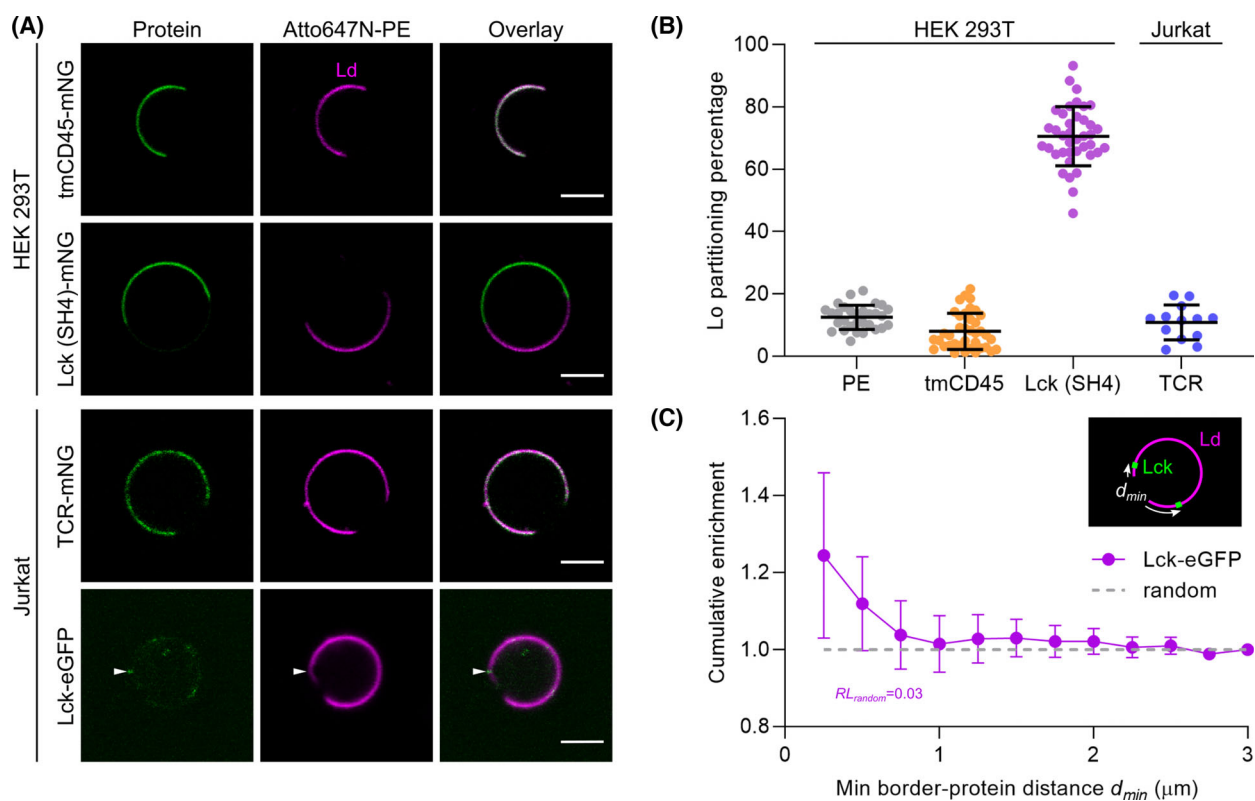

Fig. 1. Partitioning of membrane proteins in phase-separated giant plasma-membrane vesicles (GPMVs). (A) Representative images of equatorial planes of GPMVs derived from HEK 293T cells expressing transmembrane domains (tm) of CD45 or membrane-binding Lck domain SH4 fused with mNeonGreen (mNG; top left, green), and from Jurkat T cells expressing TCR-mNG or Lck-eGFP (bottom left, green). GPMVs were stained with a liquid-disordered (Ld) phase marker (fluorescent lipid analogue Atto647N-PE, magenta, central column; scalebar: 5 μm). The arrow in the bottom panel indicates protein signal at the border of the lipid phases; see more examples in Fig. S3. (B) Liquid-ordered (Lo) phase partitioning percentages (determined as illustrated in Fig. S1) for selected proteins and the Ld phase marker (PE) as the Ld control. Every data point represents a value from a single GPMV, and the bars indicate the means and standard deviations. (C) Cumulative enrichment of distances between lipid-phase borders and nearest Lck-eGFP entity (d_{min}, as illustrated in the inset and exemplified in Fig. S3C,D) in Jurkat GPMV; values >1 indicate above-random occurrences. The relative likelihood value indicates the probability that the data arose from a random distribution without border enrichment (RL_{random}; see Methods for details).

residue, the mutation resulted in a complete abolishment of the Lo partitioning. A similar effect was observed for one of the two cysteine sites of LAT in accordance with the literature [3], whereas, interestingly, for Lck (SH4) mutation of both cysteine sites induced only a modest reduction in the preference for the Lo phase, likely owing to its additional myristoylation. We obtained consistent results with GPMVs using DTT/PFA, which cleaves off palmitoyl [3], but not myristoyl groups [41].

Interestingly, the full-length Lck-eGFP construct could not enter the Lo phase in GPMVs of either Jurkat or HEK 293T cells, but was frequently found at the border of the two phases (Fig. 1A bottom and Fig. S3A, where some instances show inadvertent protein aggregation). The increased occurrence of the protein signal at small distances from the phase border (Fig. 1 C) showed low relative likelihood that the data arose from a random protein distribution without border enrichment (RL_{random}; see Methods for details). Such border enrichment has previously been observed for some proteins in simulations [42] and experimentally [43]. This behaviour indicates a slight mismatch of the molecule (and/or its aggregates) with the disordered lipid phase under the imposed conditions. Given the artificially dense packing of the ordered phases at the low temperatures used in our model system, we speculate that such border partitioning could be the manifestation of a tendency towards more ordered membrane environment under more physiological conditions, as corroborated by further experiments below.

While the T cell-activating proteins Lck, CD4, and LAT prefer the ordered membrane environment, their key antagonist tmCD45 and the TCR prefer the opposite (Fig. 1B), as do transmembrane domains of an inhibitory receptor CTLA-4, a costimulatory receptor CD28, and its ligand CD86 (Fig. S2A). For TCR, conflicting results had been reported: Ld partitioning, as observed here, was observed in model membranes [29, 30] and sometimes in resting T cells [17, 18], whereas most of research especially with activated T cells concluded its preference for the highly ordered lipid phase [17–22].

Partitioning of protein aggregates in phase-separated GPMVs

To resolve this discrepancy, we next isolated GPMVs from Jurkat T cells that had previously been activated by an anti-CD3 antibody (OKT3) in solution, inducing aggregation of the TCR. Interestingly, the induced TCR aggregates were frequently observed at the boundary between the two lipid phases (Figs 2A and S4A). Though the remaining signal of nonclustered TCR precluded quantitatively significant border enrichment (see the comment in Methods), the time-lapse images (Fig. 2A) attest the high affinity of some TCR aggregates for the phase boundary. The indicated change in the preference of the activation-induced TCR aggregates away from the disordered membrane environment is in line with previous observations [17–22].

We next checked whether the change in the lipid-phase preference of the TCR upon T-cell activation was caused by an active cellular process or merely as a passive consequence of protein cross-linking. To this end, we derived GPMVs from nonactivated Jurkat T cells and verified the lipid-phase partitioning of TCR cross-linked by primary (OKT3) and secondary antibodies. These TCR aggregates frequently partitioned to the lipid-phase boundary (Figs 2B,D and S4B). Noteworthy, OKT3 alone did not induce appreciable aggregation of TCR in GPMVs derived from nonactivated T cells (Fig. S5), which indicates that some TCR aggregates observed in GPMVs from preactivated cells were likely additionally stabilised by other proteins and/or coalescence of ordered lipid domains.

Cross-linking of TCR thus seemingly changed the protein's preference for the lipid environment, which could result from a conformational change of the protein, or simply from a more general molecular change imposed by aggregation, such as reduced mobility or molecular crowding effects. We therefore examined the partitioning of another Ld-preferring protein, CD45, aggregated with antibodies after isolation of GPMVs – a clearly unnatural condition without a biological function. Interestingly, CD45 aggregates also showed enriched localisation at the border of lipid phases (Figs 2C,D and S4C), highlighting that aggregation of different Ld-partitioning proteins can drive their preference away from the disordered lipid environment in a completely passive way. We also verified that the effect was not due to a specific property or component of the membranes from T cells: we expressed TCR in Chinese hamster ovary (CHO) cells and therefrom derived GPMVs, in which antibody-aggregated TCR also showed frequent border partitioning (Fig. S4D).

In the experiments above, not all proteins settled at the phase boundary. Noteworthy, the phase separation reduced its total length, for which many protein species might compete, as well as increased the time needed for the diffusion-limited process to reach the equilibrium. In addition, we induced large-scale phase separation in GPMV membranes by cooling the sample to 4 °C and addition of the chemical DCA. Such membrane system is commonly used as an
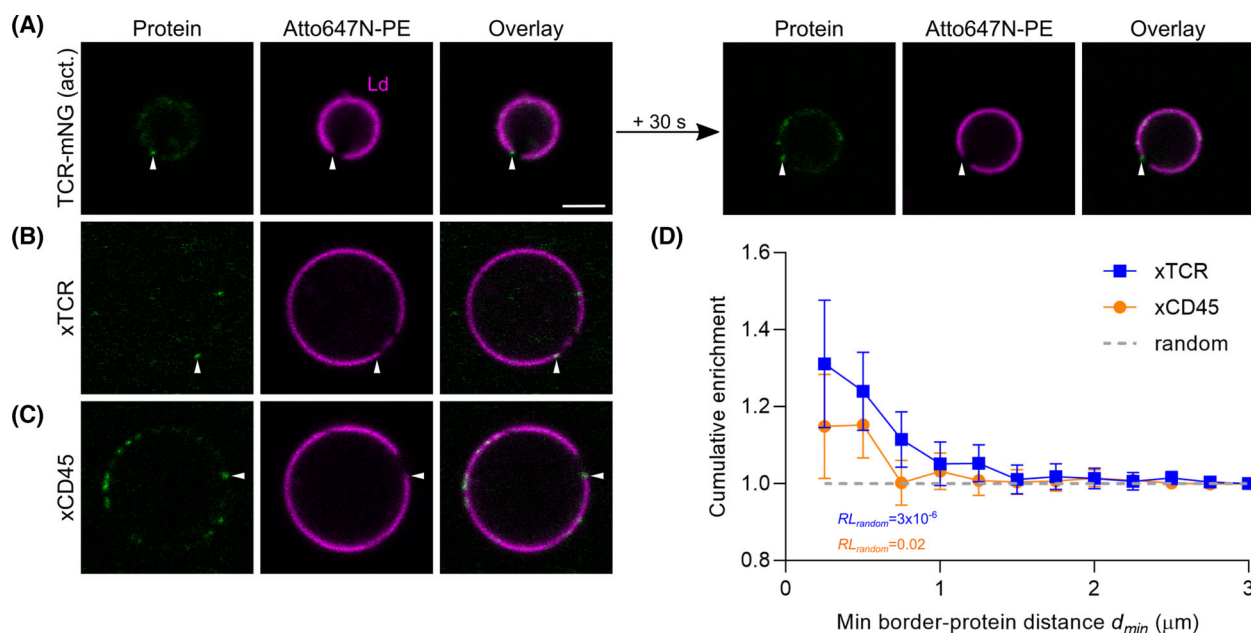
Fig. 2. Partitioning of protein aggregates in phase-separated GPMVs. (A–C) Representative images of equatorial planes of GPMVs derived from Jurkat T cells, stained with the liquid-disordered (Ld) phase marker – fluorescent lipid analogue Atto647N-PE (magenta, central column), with aggregated proteins (green). (A) TCR-mNG was aggregated in live cells during their activation with OKT3 in solution before the formation of GPMVs. Right: images of the same vesicle 30 second later, indicating that protein aggregates stick to the lipid-phase border. (B,C) Nonfluorescent proteins were artificially cross-linked (xTCR, xCD45) in GPMVs by incubating with primary (OKT3 against TCR, Gap8.3 against CD45) and fluorescently labelled secondary antibodies. Arrows point at proteins localised at the border of lipid phases; see more examples in Fig. S4. (D) Cumulative enrichment of distances between lipid-phase borders and nearest aggregates of TCR (blue) and CD45 (orange) in Jurkat GPMVs; values > 1 indicate above-random occurrences. The relative likelihood value indicates the probability that the data arose from a random distribution without border enrichment (RL_{random}; see Methods for details).

experimentally convenient model believed to mimic physical and chemical properties of nanoscale membrane heterogeneities in GPMVs [44] and live cells under physiological conditions [31, 37]. However, the packing densities and diffusion rates were clearly affected by low temperature [45] and addition of chemicals [46], which could affect the preference of protein aggregates for a specific membrane state. Though the observed occasional border localisation may be condition-dependent, and quantitative evaluation not always conclusive, it initiated our further investigations of the membrane environment around protein aggregates with complementary techniques.

Membrane order around protein aggregates in GPMVs

We next aimed to verify whether any local ordering could be detected at the sites of protein aggregates in GPMV membranes at room temperature and without DCA, which seem homogeneous on spatiotemporal scales of confocal microscopy but have recently been reported to also exhibit nanoscale heterogeneities [44].

To this end, we stained the vesicles with a polarity-sensitive membrane dye NR12S [47, 48], which shifts its emission spectrum towards longer wavelengths in more disordered membrane environment. Spectrally resolved imaging (Fig. S6A) allowed subsequent unmixing of the overlapping signal contributions from the protein and NR12S as well as determination of its spectral peak position (λ_{MAX}) by spectral fitting (Fig. S6B) in every pixel of the image (Fig. 3A) [49]. At the sites of both TCR and CD45 aggregates, the fluorescence of NR12S was on average slightly shifted to shorter wavelengths (Figs 3B and S6C), indicating that protein aggregates can locally induce a more ordered lipid environment. This has been previously demonstrated also by patching of membrane proteins (including CD45) in Jurkat T cells [50]; with this study on GPMVs, we can confirm this is a passive process. We detected a similar effect also for TCR aggregates in GPMVs derived from CHO cells (Fig. 3B), again excluding the possibility of the phenomenon being specific to T cells.

The observed 1–2 nm average spectral shift is small, but consistent and thus statistically significant (Fig. 3
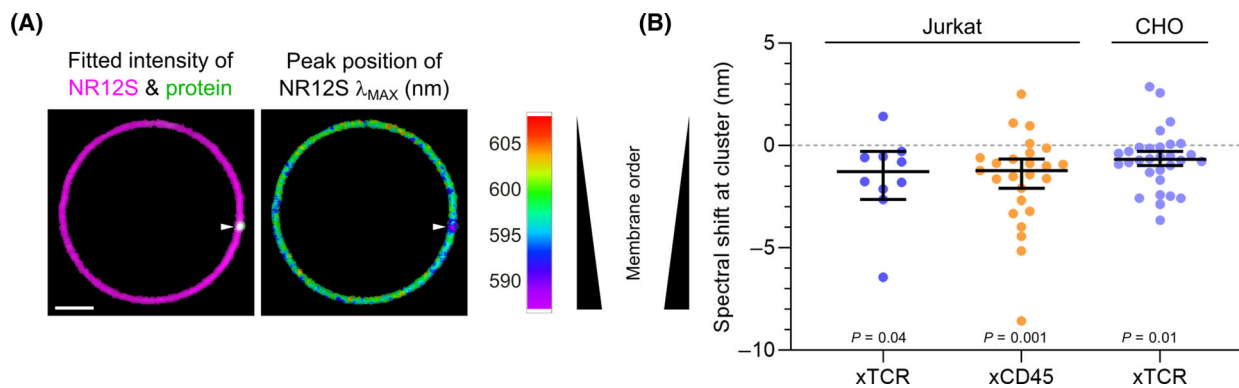
Fig. 3. Membrane order in GPMVs with proteins aggregated by antibodies. (A) Spatial maps of the fitted intensities (left) of the protein-aggregating antibody (green; a protein cluster indicated by the white arrow) and of the polarity-sensitive membrane probe NR12S (magenta), together with its spectral peak position (λ_{MAX}, right; colour scale depicted: lower values indicate a more ordered membrane environment; scale bar: 2 μm). (B) Difference in the spectral peak position (i.e. spectral shift) of NR12S between the sites of identified protein clusters and the rest of the membrane ($\lambda_{MAX,at\ protein} - \lambda_{MAX,elsewhere}$), for cross-linked TCR and CD45 (xTCR and xCD45, respectively) in GPMVs from Jurkat T cells, and for TCR aggregates in GPMVs from CHO cells. Please note that local differences may be greater, but were partially averaged out by confocal resolution. The data are from a representative biological repeat; each dot corresponds to one identified protein cluster and bars indicate medians and their 95% confidence intervals. The *P*-values for each sample were calculated by a two-sided *t*-test against the hypothetical mean value of 0. For details, see Methods and Fig. S6.

B). One should also bear in mind that the images were recorded with confocal resolution, which likely exceeds the size of the protein aggregates and thereby of the induced regions of increased lipid order, meaning that the real local shifts recorded on smaller scales would be proportionally larger. In phase-separated GPMVs from Jurkat T cells, the difference between the spectral emission peaks of NR12S in both phases is around 15 nm (Fig. S7). Assuming a similar spectral response of the dye in nanoscale cellular heterogeneities, we can estimate the average size of the induced more ordered regions to a tenth of the axial confocal cross-section (i.e. 100–150 nm), which is not unreasonable for an aggregate of multiple cross-linked proteins.

Membrane order around immobilised proteins in live T cells

Above, we have used GPMVs as model membranes to investigate the preference of membrane proteins for, and their influence on, the local membrane environment. Though GPMVs pertain most of the compositional complexity of the plasma membrane [35] and are thus believed to be the most relevant passive mimicking system, certain key structural properties are nevertheless eliminated during their formation, such as interleaflet asymmetry [36] and interactions with the cytoskeleton [51]. To verify whether our observations translate also to live cells, we next investigated the local lipid order at the sites of the proteins of interest

in Jurkat T cells. Spectral imaging with the polarity-sensitive dye and spectral fitting were again employed to concurrently devise maps of protein density (Fig. 4A, central column, green) and membrane polarity, reporting on the local lipid order (Fig. 4A, right column). Through the detected spectral shifts of NR12S at the sites of high protein density with respect to the rest of the membrane, variations in the lipid environment of proteins were examined. By filtering of pixels according to the protein intensity relative to the local NR12S intensity, we reduced the influence of bright spots enriched with both protein and lipid signal (e.g. vesicles), allowing us to increase the sensitivity to subtle spectral differences stemming from subresolution features (please see Methods for details).

When Jurkat cells were activated on an OKT3-coated surface, Lck and CD45 coincided with more ordered and disordered membrane environments, respectively (Fig. 4B), which is in line with the measurements of nonaggregated proteins in GPMVs (Fig. 1). TCR, in contrast, now showed a tendency towards more ordered membrane regions than CD45 (Fig. 4B), corroborating the change of its preference seen upon cell activation or aggregation, observed in the model systems above.

In GPMVs, we observed very similar membrane remodelling by aggregates of both TCR and CD45, potentiating a general passive underpinning molecular mechanism. To further verify whether similar membrane ordering effects could be exhibited in live T cells
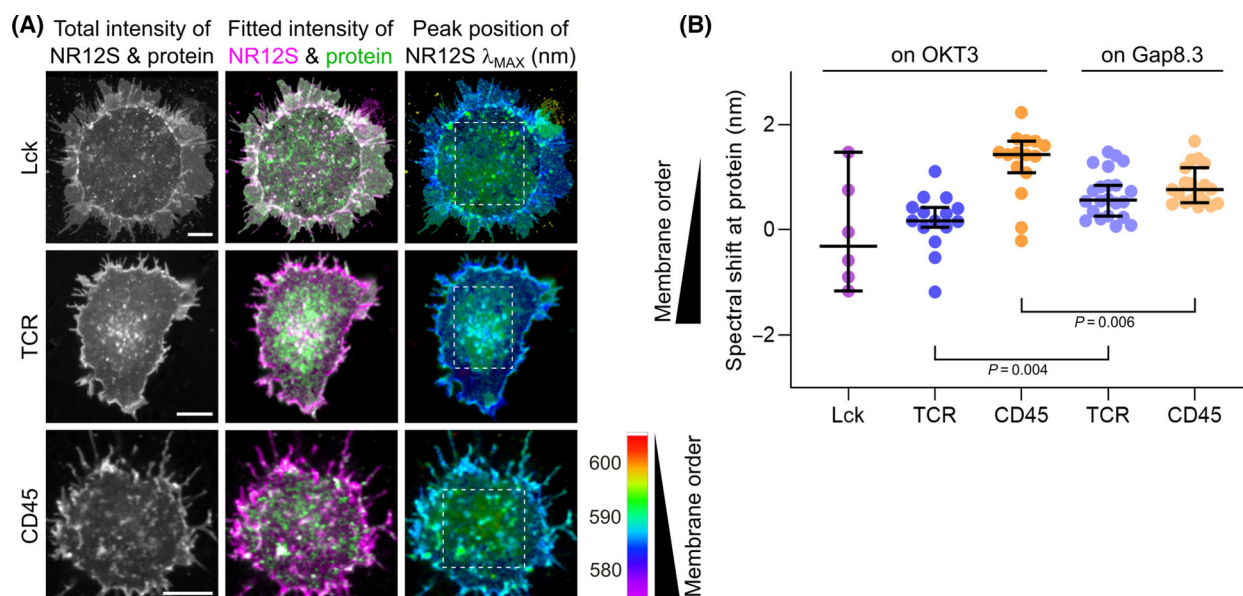
Fig. 4. Membrane order in Jurkat T cells on antibody-coated glass surface, probed *via* spectral imaging with a polarity-sensitive membrane probe NR12S. (A) Representative images of live Jurkat T cells activated on OKT3-coated surfaces: overall intensity (left column), spectrally decomposed intensities of the protein (central column, green; Lck-eGFP (top row), TCR (middle), and CD45 (bottom) labelled with a fluorescent antigen-binding fragment) and NR12S (magenta), and its peak position (λ_{MAX}, right column; colour scale depicted: lower values indicate more ordered membrane). The areas within the white dashed rectangles were used to calculate the (B) relative spectral shifts of NR12S in the membrane regions with high protein signal, compared with the rest of the membrane for each cell, for Jurkat T cells activated on surface coated with OKT3 (anti-CD3) or Gap8.3 (anti-CD45). Every data point represents a single cell from the same representative biological replicate, and the bars indicate medians and their 95% confidence intervals. Please note that local differences may be greater, but were partially averaged out by confocal resolution. The *P*-values were obtained using the two-tailed Mann–Whitney nonparametric test.

as well, we repeated the last experiment by dropping the cells on a Gap8.3-coated surface to immobilise CD45 proteins. In this case, the local membrane order around CD45 increased compared with the previous experiment with an OKT3-coated surface (Fig. 4B), whereas the ordering at nonengaging TCR was now slightly released. Though the differences are small, we checked that they do not arise from energy transfer between the two dyes or imperfect spectral unmixing (see Fig. S8 and comments in Methods). As the primary antibodies on the surface cannot substantially aggregate the targeted proteins, these results imply that immobilisation of a membrane protein can locally induce a more ordered membrane environment in live cells also without excessive large-scale aggregation, reported previously [50].

In the experiment above, full immobilisation of the protein engaging with surface-bound antibodies was employed, which is certainly a simplistic setting and may have exaggerated the observed effects. In a physiological case, the interaction of TCR and coreceptors with a peptide-loaded major histocompatibility complex (pMHC) on an antigen-presenting cell with a fluid plasma membrane would slow down the protein aggregate [52], but not to a complete stall.

Coming a step closer to a realistic scenario while keeping well controlled conditions and planar geometry suitable for microscopy of the interface, we substituted the antibody-coated surface with a supported lipid bilayer (SLB) – a fluid artificial membrane deposited on a coverslip. The SLBs were decorated with diffusing molecules of CD58 [53], which binds to the adhesion protein CD2 on the surface of T cells and thereby reduced their crawling while imaging, but did not promote their spreading (Fig. 5A, top row, 'adh'). To prompt the engagement of TCR with the SLB, we either incorporated pMHC (Fig. 5A, bottom) or labelled TCR with an anti-CD3 antigen-binding fragment (Fab) with a large extracellular protein domain (UCHT-1 fused to CD45R0) possessing a His-tag group (Fig. 5A, middle row, 'TCR-His'), which binds nickel-nitrilotriacetic acid (Ni-NTA)-functionalised lipids in the SLB. None of these conditions would explicitly promote cross-linking of TCR.

Compared with the case with no specific TCR engagement with the SLB ('adh'), TCR binding to SLB *via* both pMHC and TCR-His induced similarly pronounced spreading of the cells (Fig. 5A), local ordering of the membrane around TCR (Fig. 5B), and slowdown of the diffusion of TCR proteins (Fig. 5C),
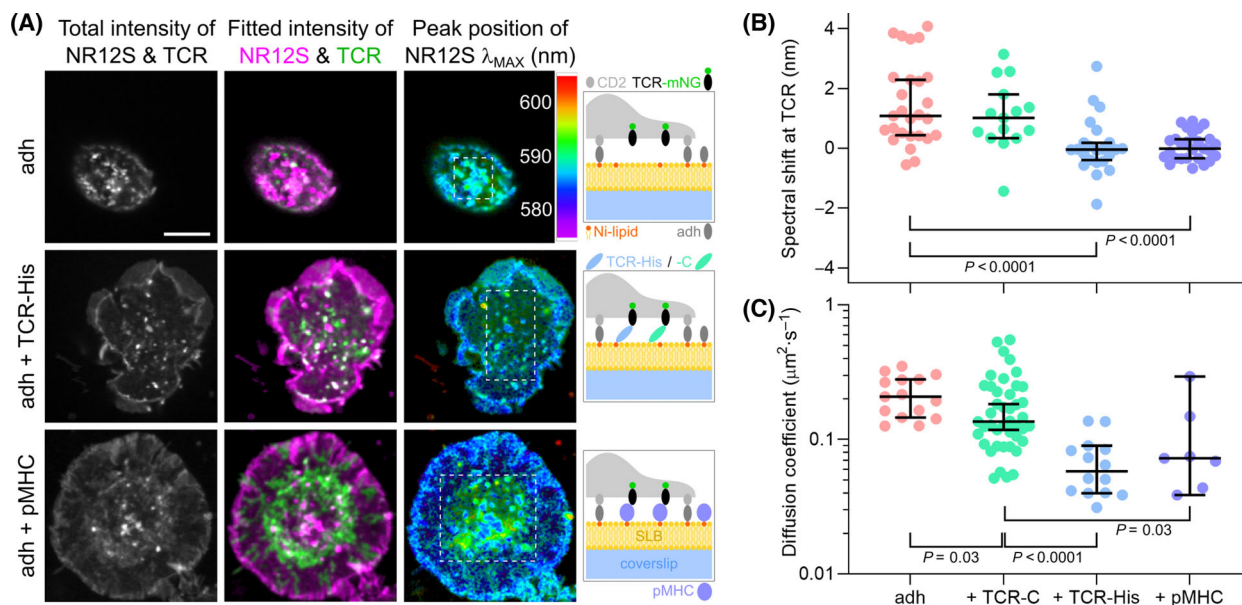
Fig. 5. Membrane order and diffusion of TCR in Jurkat T cells on supported lipid bilayers (SLB). (A) Sample images of live Jurkat T cells expressing TCR-mNG: overall intensity (left column; scalebar: 5 μm), spectrally decomposed intensities of the TCR (central column, green) and polarity-sensitive membrane dye NR12S (magenta), and its peak position (λ_{MAX}, right column; colour scale depicted, lower values indicate more ordered membrane). Cartoons depict experimental conditions: all SLBs were decorated with the adhesion protein CD58 (adh) to attach the cells for imaging. TCR was made to interact with the SLB *via* the pMHC complex on the SLB (bottom row), or *via* an anti-CD3 Fab with a His-tag (TCR-His) that binds nickelated (Ni-) lipids in the SLB (middle row). The areas within the white dashed rectangles were used to calculate the (B) relative spectral shifts of NR12S in the membrane regions with high protein signal, compared with the rest of the membrane of each cell. Please note that local differences may be greater, but were partially averaged out by confocal resolution. (C) Diffusion coefficient of the TCR-mNG in its high-density regions in Jurkat cells on SLBs under different conditions (TCR-C: TCR labelled with a C-tag Fab, which does not bind to lipids in the SLB), obtained with FCS. Every data point represents a single FCS recording, acquired at a different location; typically, 2–4 positions per cell were measured. In B and C, the bars indicate medians and their 95% confidence intervals. The *P*-values, comparing data from the same representative biological replicate, were obtained using the two-tailed Mann–Whitney nonparametric test.

measured by fluorescence correlation spectroscopy (FCS) in regions of the cell with the highest TCR density (e.g. aggregates). A similar Fab with the His-tag substituted by a C-tag ('TCR-C'), unable to bind the opposing SLB, slowed down TCR considerably less (Fig. 5C) and induced no detectable local membrane ordering (Fig. 5B). This shows that an approximately threefold–fourfold reduction in diffusivity corresponded to a comparable change in local membrane order as for immobilised or cross-linked proteins (Figs 3B and 4B, respectively).

Noteworthy, both conditions with slow down-induced membrane ordering (i.e. SLB with pMHC and TCR labelled with the His-tag, but not the C-tag Fab) also elicited robust T-cell triggering, as probed by cytosolic calcium release (K. Y. Chen *et al.*, submitted). Though the increased membrane ordering around TCR is linked with activation of the cells, we cannot firmly determine the direction of causality, as our measurements were performed several minutes after landing of the cells and thus well after their activation.

Nevertheless, light-induced intracellular cross-linking of the TCR has recently been shown to directly induce activation of T cells [54]. Furthermore, our findings with live-cell microspectroscopy importantly corroborate very similar observations with super-resolution microscopy with fixed B cells [31, 32], implying common underlying molecular mechanisms. To evaluate the possibility of involvement of lipid reordering in the activation process, as suggested by simulations [31, 32], we reverted to a passive membrane model system, discussed next.

Colocalisation of Lck with protein aggregates in GPMVs

T-cell activation relies on TCR being phosphorylated by Lck. Our results, described above, indicate that in the resting state with both proteins freely diffusing, the frequency of their random encounters could be kept low also by their intrinsic preference for different type of local membrane environment. However, upon

engagement of TCR (and its coreceptor CD4) with pMHC, leading to the slowdown of the protein aggregate (Fig. 5C), the modified local membrane order (Fig. 5B) resembled more the preferred environment of the Lck (Fig. 4B), potentially fostering their interaction required for the triggering to occur.

The polarity-sensitive dye, used so far, can only report on the similarity of the local lipid order of the membrane patches created by protein immobilisation and those hosting Lck, but cannot reveal their identity or interactions. To finally verify whether these lipid heterogeneities can mediate the attraction between the proteins, we investigated colocalisation of Lck with antibody-induced aggregates of TCR in GPMVs – a passive model membrane system devoid of cellular processes. Despite weak signals, owing to low incorporation of Lck into the GPMVs and down-regulation of TCR in the cell line overexpressing fluorescent Lck, we observed many occurrences of its coincidence with TCR aggregates (Fig. 6A), as speculated earlier [50]. We confirmed the relevance of this colocalisation by a quantitative analysis of the extracted two-colour intensity profiles along the membrane (Fig. 6B; the Overlap intensity ratio Z score measures the increase in signal colocalisation compared with randomly scrambled intensity profiles - values above 0 indicate an above-random degree of colocalisation; see Methods for details). We verified that the aggregates did not attract all the membrane components in an unspecific manner, as the membrane dye Atto647N-PE did not show any enrichment at the sites of protein aggregates (Figs 6B and S10A).

Interestingly, but perhaps not anymore unexpectedly, Lck was recruited also by the aggregates of CD45 molecules (Fig. 6A,B), which induced increased lipid ordering in GPMVs similarly as aggregates of TCR (Fig. 3B). Moreover, even the aggregates of only the transmembrane domains of CD45 or CD86 were able to attract Lck (Fig. 6C,D) as well as its membrane-binding domain SH4 (Fig. S11). This diminishes the possibility of the observed colocalisation being the consequence of binding between intracellular protein domains and invigorates the involvement of lipid-mediated interaction between the proteins upon external modulation of their mobility, here imposed by aggregation.

Interplay of energy and entropy in lipid–protein interactions

The similarity in behaviour between aggregates of TCR and CD45, which both locally induce ordered lipid environments and attract Lo-associated Lck, as do cross-linked transmembrane domains of CD45 and

unrelated CD86, hints towards a rather general biophysical mechanism at play. This notion can find broader support in numerous studies on lipid–protein interactions [5]. For instance, simulations have shown that lipids in shells extending 3–4 nm around membrane proteins exhibit reduced mobility and increased order, exacerbated by protein oligomerisation [55], immobilisation [56], or crowding [57], which can result in nucleation of larger-sized ordered regions. It has indeed been shown experimentally that immobilisation of Lo-partitioning proteins can stabilise ordered membrane environments [58]. Furthermore, cross-linking of lipids can change their phase partitioning towards more ordered environment [59], which can also be induced by immobilisation of certain lipid species [45, 60]. In cells, the effect of such immobilisation can extend across to the opposing leaflet to assure coregistration of lipid ordering [61]. This all indicates that protein oligomerisation, diffusion, and lipid ordering are indeed tightly linked *via* passive biophysical concepts and corroborates our findings that aggregation-induced partial immobilisation and consecutive lipid ordering can modulate lipid-mediated interactions between proteins (Fig. 6).

We finally aimed to roughly assess whether this mechanism can apply also to partial immobilisation of a single nonclustered protein molecule, as in ligand binding to the receptor, which would extend the concept of pinning as a mechanism to nucleate membrane nanodomains [62]. The observed threefold to fourfold slowdown of TCR (Fig. 5C), comparable also to the reported relative difference in diffusivity between the Lo and Ld phases in model membranes [63, 64], reduces its translational entropy, which is paid for by the receptor-ligand binding energy. Simultaneously, the surrounding lipids are slowed down by a similar degree, which corresponds to a reduction in their translational entropy [65, 66] by 1–1.5 k_B per molecule ($\Delta S_t = k_B \ln(D_{slow}/D_{free})$, with ΔS_t being the translational entropy change due to the change in mobility, k_B the Boltzmann constant, and $D_{free,slow}$ the diffusion coefficients of the freely moving and slowed-down molecules). For the lipids around bound/aggregated proteins to retain the equilibrium of the free energy (F) with lipid molecules in the shells of unrestrictedly moving proteins ($F_{slow} = F_{free}$), the additionally slowed-down lipids need to compensate this reduction in translational entropy by reducing their energy levels accordingly ($\Delta E = T\Delta S$, with ΔE being the reduction in energy due to the entropy reduction ΔS, with constant temperature T). The lipids can achieve such energy reduction by stronger Van der Waals attraction between alkyl chains upon
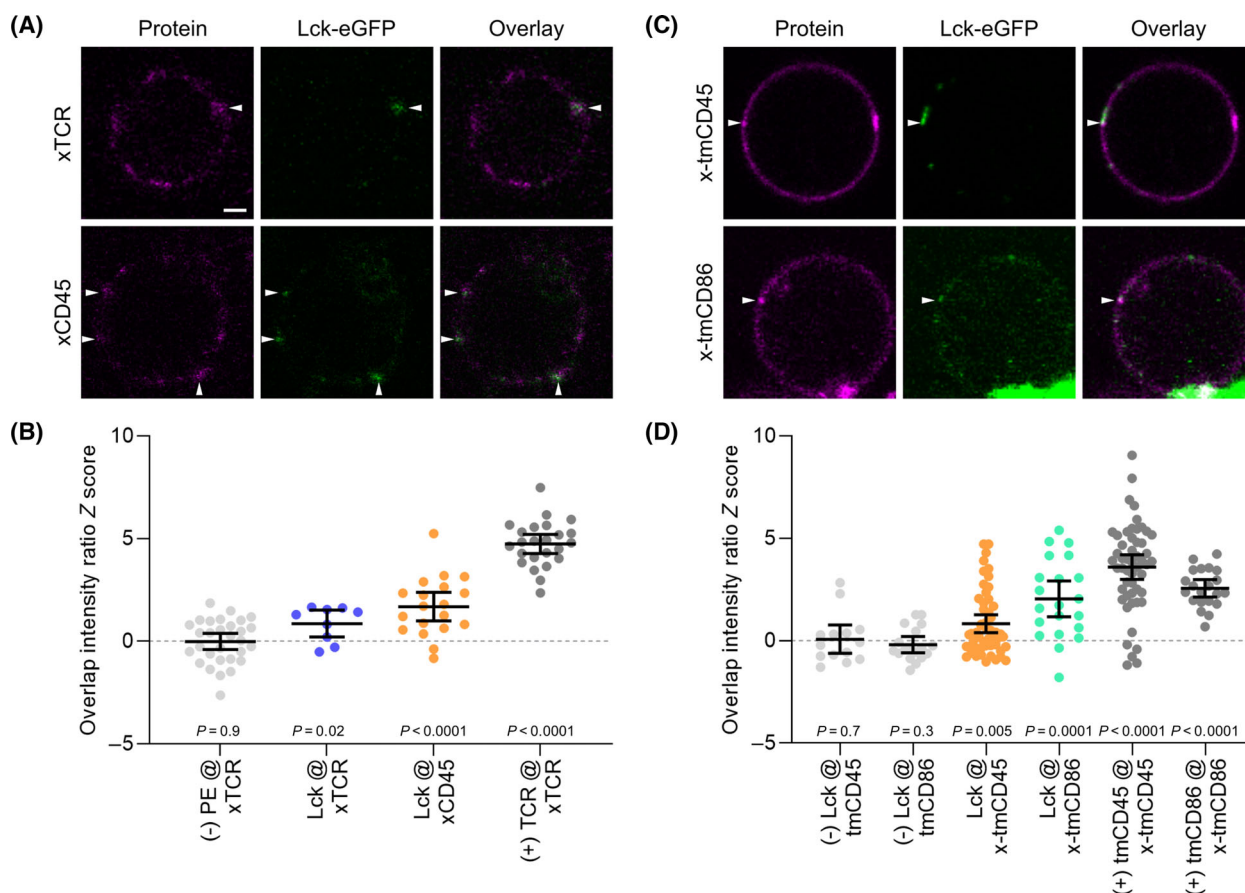
Fig. 6. Colocalisation of Lck with protein aggregates in GPMVs. (A) Representative images of equatorial planes of GPMVs derived from Jurkat T cells expressing Lck-eGFP (green), with TCR (top) or CD45 (bottom) cross-linked with primary (OKT3 and Gap8.3, respectively) and fluorescently labelled secondary antibodies (magenta; scalebar: 2 μm). Arrows point to the sites of Lck colocalising with a protein aggregate. From the extracted two-colour intensity profiles along the membrane, (B) the Overlap intensity ratio z-score was calculated (values > 0 indicate above-random colocalisation; see Methods for details). As the positive and negative control (+/-), colocalisation of the TCR aggregates with TCR-mNG (TCR) and Atto647N-PE (PE) was investigated, respectively (images in Fig. S10). Every data point represents an intensity profile along the vesicle perimeter, images are from the same representative replicate; the bars indicate means and their 95% confidence intervals. The *P*-values for each sample were calculated by a two-sided t-test against the hypothetical mean of 0 (all samples passed the normality tests). (C) As A, with transmembrane domains of CD45 and CD86 fused to fluorescent mRuby3, cross-linked with primary and fluorescent secondary antibodies. (D) As B, with nonaggregated proteins and self-colocalising aggregates as negative and positive controls (-/+). The *P*-values for each sample were calculated by the Wilcoxon sign-rank nonparametric test against the hypothetical median value of 0.

tighter packing. As the increased order also reduces the conformational entropy of lipids [66, 67], the corresponding energy decrease in $\Delta E = 1–1.5\ k_B T$ per molecule is likely an underestimate. Even as such, this ΔE already exceeds the line tension-related demixing enthalpy needed to induce local phase separation (around $0.5–1\ k_B T$ per molecule) [6, 64]. Taking into account that the shell of each protein contains tens of affected lipids, their collective contribution can overcome the energetic penalty of the protein in unfavourable lipid environment, which is on the order of $2\ k_B T$ per protein [4].

In this crude back-of-the-envelope magnitude estimation of the thermodynamic effects, which would merit deeper theoretical and experimental exploration, the observed degree of the slowdown of a membrane protein could suffice to locally nucleate a more ordered lipid environment. Even as lipids dynamically exchange on a short time scale, these immobilisation-induced membrane patches represent an energetically favourable environment for membrane proteins that preferentially partition into ordered phases due to the length of their transmembrane domain and lipidation, such as Lck. Such attraction potentiates higher rates

of their interaction with the ligand-bound membrane proteins than their freely moving copies. In the fair democracy of thermodynamics, the numerosity of lipid–protein and lipid–lipid interactions can thus provide a significant lever to orchestrate the nanoscale membrane organisation, which participate in membrane-hosted events such as signalling.

Further implications for cellular processes

Our data corroborate that membrane proteins can vary their preference for different lipid environments according to external changes. We have shown that membrane proteins that individually partition into disordered lipid environments, such as TCR or CD45, can upon aggregation or partial immobilisation shift their preference towards more ordered membrane parts. This could possibly be initiated already by ligand binding, as we attempted to demonstrate with slowing down the TCR by binding to lipids in supported lipid bilayers. Unfortunately, we could not directly follow the molecular events during the very early stage of T-cell activation, as the required temporal resolution at single-molecule sensitivity is unattainable to the currently available live-cell microspectroscopy techniques. Furthermore, we conducted our measurements only 5–10 min after the cell-surface contact to avoid potential bias of the readouts owing to nonplanar topography of the initial contact sites [68], during which cell activation could have induced additional aggregation of TCR. However, as simulations predict that the local lipid composition and order respond to immobilisation of a membrane protein within microseconds [42], this lipid–protein interplay may represent the very first subtle, though likely not decisive, membrane response in sensing of external binding.

We can speculate that the newly acquired tendency of the engaged TCR for more ordered lipid environment is further enforced by aggregation with the Lo-preferring coreceptor CD4 (Fig. S4A), which additionally facilitates interactions with positive regulators Lck and LAT (Fig. S4A), as we observed in our passive model system with GPMVs (Fig. 6). The tightly packed membrane embedding also slows down the diffusion of the engaged protein complex through the close contact zone to promote phosphorylation [69]. Furthermore, primary T cells with more ordered membrane, which is more prone to phase separation, have been found to form more stable immune synapses [70]. The induced ordered regions can then further facilitate association with the cytoskeleton [50, 71, 72] needed for the translocation of the engaged and aggregated receptors for further processing and recycling.

Our findings therefore indicate that the key molecular events of the kinetic-segregation model of T-cell activation [11] could be accompanied by consistent changes in the membrane environment, supporting the sensitive and specific response of each T cell. However, from the presented data we cannot attest whether the seen effects can in any way assist the activation, or they arise as its side effect. It therefore remains to be quantified whether the observed membrane remodelling affects the frequency of the earliest interactions between the investigated proteins, as well as with other negative regulators, such as Lck-inactivating protein Csk (PAG) [4] and SHP-1 [73] that also partition into ordered membrane environments. These formidable experimental challenges will eventually be overcome by advances on both the imaging/spectroscopy part [74, 75] as well as on the side of well controlled cell-activating systems [76]. Such progress will help to determine the degree to which the suggested lipid-mediated binding recognition upon receptors' immobilisation can influence the final signalling outcome, and perhaps its relation to malfunctions such as immune disorders.

Similarities of molecular machinery employed in other cell types will enable a direct translation of these findings to other signalling events, in particular to the triggering of B lymphocytes, which involves phosphorylation of B-cell receptors (BCR) controlled by the kinase Lyn and phosphatase CD45. Remarkably, it has recently been shown by super-resolution microscopy of fixed B cells that during this process, aggregation of the BCR, itself preferring disordered membrane environment, promotes accumulation of more ordered lipid regions, recruitment of thereto-partitioning Lyn and exclusion of CD45 [31, 32]. This process is largely powered by lipid–lipid interactions for soluble antigen [31] and additionally enhanced for surface-bound antigens [32]. Similar parallels could be drawn also to the activation of other cascades that knowingly depend on lipid heterogeneities, such as FcεRI-mediated IgE signalling in mast cells [33, 34], giving our findings widespread implications for membrane-hosted events.

Methods

Plasmids

For transient transfections, a pHR plasmid backbone was modified to contain a BamHI-MluI-SpeI-NotI multiple cloning site. A Kozak sequence, signal peptide, HA tag and GGSG linker were added between BamHI and MluI. Full length CD28 (aa 19-220, UniProtKB P10747) and

CTLA-4 (aa 36-223, UniProt P16410) were cloned between MluI and SpeI. Similarly, the transmembrane (tm) domains of human CD4 (aa 391-423 UniProtKB P01730), CD45 (aa 573–608, UniProtKB P08575), CD86 (aa 243-277, UniProtKB P42081) and LAT (aa 1-35, UniProtKB P43561), and their mutants, were cloned between MluI and SpeI, and for all constructs fluorescent protein mNeonGreen (mNG) or mRuby3 between SpeI and NotI. Lck (SH4 domain) and mutants were cloned between BamHI and SpeI with only a Kozak sequence. For stable cell lines, using a pHR plasmid backbone, mNG was fused to the C terminus of the beta chain of a high-affinity gp100 specific TCR (kind gift from Immunocore Ltd.), and eGFP to the C terminus of wild-type human Lck (UniProtKB P06239).

Cell culturing and transfections

Adherent HEK 293T cells (CRL-3216, ATCC), and derivatives, were grown in T75 flasks (CELLSTAR by Greiner Bio-One, Kremsmünster, Austria) with DMEM (D5796, Sigma-Aldrich, St. Louis, MO, USA) supplemented with 10% foetal bovine serum (FBS; Gibco by Thermo Fisher, Waltham, MA, USA), 2 mM L-glutamine and 1% penicillin-streptomycin (all from Sigma-Aldrich). Jurkat T cells (ATCC), and derivatives, were cultured in T25 flasks (CELLSTAR) with RPMI (1640, Thermo Fisher) supplemented with 10% FBS (Gibco), 10 mM HEPES, 2 mM L-glutamine, and 1% penicillin-streptomycin (all from Sigma-Aldrich). HEK 293T and Jurkat cells were grown at 37 °C and 5% CO_2. Suspension Chinese hamster ovary cells (FreeStyle CHO-S cells, R80007, Thermo Fisher) were kept in suspension in plastic Erlenmeyer shake flasks (Corning; Corning, NY, USA) with FreeStyle CHO Expression Medium (12651022, Thermo Fisher) supplemented with 8 mM L-glutamine (Sigma-Aldrich) under 37 °C, 85% humidity, and 8% CO_2 on an orbital shaker at 125 rpm. All cells were free of mycoplasma.

Lentiviral production and transduction were used to generate stable Jurkat cell lines expressing gp100-reactive TCR-mNG, Lck-eGFP or Lck (SH4)-mNG, and CHO-S cells expressing nonfluorescent TCR, additionally assured with fluorescence-assisted cell sorting. For transient transfection of membrane proteins, HEK 293T cells were first seeded into 6-well plates, coated with poly-L-lysine (Sigma-Aldrich), one day prior to transient transfection using 0.5 μg of DNA per well and GeneJuice (Merck Millipore, Burlington, MA, USA) as per the manufacturer's instructions, and left incubating for another 2–3 days before GPMV preparation.

Preparation of giant plasma-membrane vesicles

For GPMVs prepared from activated T cells, these were first incubated in HEPES-buffered saline (HBS; 10 mM

HEPES, 150 mM NaCl; pH 7.4) with 10 μg·mL^{-1} OKT3 anti-CD3 antibody (kindly provided by the MRC Human Immunology Unit, WIMM) for 3 min at room temperature, followed by the GPMV formation procedure, described below.

GPMVs from adherent HEK 293T cells, or Jurkat and CHO cells in suspension, were prepared following the established protocol [35] with the necessary modifications for suspension cells [51]. Cells were first preswelled by washing in 30% GPMV buffer (10 mM HEPES, 150 mM NaCl, 2 mM CaCl2; pH 7.4), followed by a 2-h incubation at 37 °C in full GPMV buffer with n-ethylmaleimide (NEM, final concentration 2 mM), or dithiothreitol (DTT, 25 mM) and paraformaldehyde (PFA, 0.07%). For this step, suspension cells were transferred into 35-mm cell-culturing plastic petri-dishes (Corning). The harvested GPMVs were then purified by spinning down the cellular debris (2 min at 1 krpm) and concentrated by further centrifugation (15 min at 10 krpm).

For subsequent aggregation of proteins in GPMVs, the vesicles were incubated at room temperature with approx. 0.1 μg·mL^{-1} of the corresponding primary antibody (OKT3 anti-CD3 and Gap8.3 anti-CD45, kindly provided by Davis laboratory [77]; both mouse anti-human) for 3–10 h, followed by another 2- to 6-h incubation with approx. 0.3 μg·mL^{-1} of a secondary goat anti-mouse antibody, bare or labelled with Alexa Fluor 488, 568, or 633 (Thermo Fisher). Transmembrane proteins with extracellular HA-group were cross-linked with Biotin anti-HA.11 Tag Antibody (BioLegend, San Diego, CA, USA) and Streptavidin Alexa Fluor 647 (Thermo Fisher). The primary antibodies alone did not elicit appreciable aggregation (Fig. S5).

Antigen-binding fragments (Fabs) and proteins for SLB decorations

cDNA encoding extracellular domain (ECD) of CD58 (residues 29–215, UniProtKB P19265), the ECD of HLA-A alpha chain (residues 25-269, UniProtKB B1PKZ1), and beta-2-microglobulin (β2M, residues 21-119, UniProtKB P61769) were ligated into pHR downstream of the sequence encoding a Kozak sequence (GCCACC) and cRPTPσ signal peptide. For the UCHT-1-CD45R0-C-tag/His-tag Fabs, the UCHT-1 variable domain sequences were obtained from a previous report [78]. Both the V_H and V_L domains were cloned into their respective pOPINVH and pOPINVL backbones. Only pOPINVH was modified to have the large protein CD45RO fused to the C terminus of the V_H constant region with either His-tag or C-tag (EDQVDPRLIDGK) at the C terminus of CD45R0. For CD58, HLA-A alpha chain and UCHT-1CD45R0-His-tag sequences a H6-SRAWRHPQ FGG-H_6 'double His$_6$' tag was added on the C terminus. Soluble pMHC (HLA-A and β2M), CD58, and UCHT-1-

CD45R0-C-tag/His-tag were produced as previously described [53, 79] (K. Y. Chen *et al.*, submitted). Briefly, the ECD of CD58 was expressed transiently in HEK 293T cells, whereas the alpha and beta chains for pMHC (HLA-A) were purified from inclusion bodies and folded in the presence of gp100 (agonist; YLEPGPVTV; GenScript). UCHT-1VH-CD45R0-C-tag/His-tag vector was coexpressed along with UCHT-1VL transiently in HEK 293T cells. Proteins were either purified using NI-NTA agarose (Qiagen, Hilden, Germany) or anti-C-tag beads. Monomers were isolated by fast protein liquid chromatography using an AKTA pure protein purification system.

Preparation of antibody-coated glass surfaces and SLBs

For immobilisation of proteins in the membrane of live cells, glass-bottom 8-well microscopy chambers (ibidi µslides, glass thickness no. 1.5) were incubated with $1 \mu g \cdot mL^{-1}$ of OKT3 or Gap8.3 and $9 \mu g \cdot mL^{-1}$ of OX7 (nonspecific anti-rat Thy1.1, kindly provided by the MRC Human Immunology Unit, WIMM) in HBS overnight at 4 °C, as applied before [28]. Prior to use, chambers were washed at least three times with HBS.

Glass-supported lipid bilayers (SLBs) were prepared using vesicle fusion [80]. Lipid mixture consisting of 98% POPC (Avanti Polar Lipids, Birmingham, AL, USA) and 2% DGS-NTA-Ni^{2+} (Ni; Avanti Polar Lipids) in chloroform were mixed in a round bottom glass flask and dried under a stream of nitrogen. The dried lipid mix was resuspended in 0.22-µm filtered PBS, vortexed, and tip sonicated for 30 min on ice to produce small unilamellar vesicles (SUVs). Glass coverslips (25 mm, thickness no. 1.5; VWR) were cleaned overnight in 3:1 sulfuric acid/hydrogen peroxide at room temperature, rinsed in MQ water, and plasma cleaned for 1 min. CultureWell 50-well silicon covers (Grace Bio-Labs, Bend, OR, USA) were cut and placed on the washed coverslips (max 4 per coverslip). SUVs were added to each well at a final concentration of $0.5 \text{ mg} \cdot mL^{-1}$ (10 µL) and left for 0.5–1 h at room temperature. Wells were washed by removing and adding 5 µL PBS five times before adding proteins at the desired density. Double His$_6$ were used to tether the proteins to the lipid bilayer *via* interaction with DGS-NTA-Ni^{2+}, providing more stable binding to SLBs than single His$_6$-tagged proteins [81]. Final concentration of protein mixes included $1 \text{ ng} \cdot \mu L^{-1}$ pMHC-gp100, or $1 \text{ ng} \cdot \mu L^{-1}$ CD58 and $1 \text{ ng} \cdot \mu L^{-1}$ pMHC-gp100. Protein mixes were incubated with the bilayer for an hour at room temperature and washed in prewarmed PBS (37 °C) five times immediately before use. Protein densities were matched to physiological levels: pMHC-gp100 (agonist) 50–100/µm^2 and CD58 300–500/µm^2. Large densities of nonagonising/nonbinding double His$_6$ pMHC were used to block unbound nickel sites. Fluorescence correlation spectroscopy (FCS) was used to relate protein concentration to density on the SLB.

Two-colour imaging of proteins in phase-separated GPMVs

For experiments with phase-separated GPMVs, the membranes were labelled with a fluorescent lipid analogue Atto647N-PE (DPPE; AttoTec, Siegen, Germany) by incubating the GPMV solution with the dye at up to $0.02 \mu g \cdot mL^{-1}$ for 5–10 min, followed by a 20-min incubation with up to 0.2 mM deoxycholic acid (DCA) to facilitate large-scale phase separation [46]. A drop of the GPMV suspension was then transferred into the observation chamber created with Vaseline between two coverslips (22 × 50 mm, thickness no. 1.5; by Menzel Gläser), which was adhered to a Peltier cooling device set to 4 °C and mounted on the microscope stage [35].

The observations were conducted using an inverted laser-scanning confocal microscope Zeiss LSM780 equipped with a 40×/1.1 water-immersion objective. Green and far-red fluorescence was excited with lasers at 488 nm and 633 nm and collected in two channels within the spectral windows of 500–590 nm and 640–700 nm. For each vesicle, a z-stack of images across the entire vesicle was collected with spacing between slices of 0.56 µm and sampling of around 0.1 µm·pixel^{-1}. Acquisition of each slice took 2–6 s (depending on the field-of-view, adjusted to the size of each vesicle, and line averaging), which was fast enough that the locations of protein aggregates were not smeared by their diffusion. It is worth noting that the proteins and aggregates located at the phase border diffused together with the lipid domain, which could result in higher accumulated signal for those entities compared with the freely diffusing protein instances. However, observation of some inadvertent Lck-eGFP multimers or aggregates in GPMVs produced with the NEM protocol (Fig. S3A) is consistent with our independent work employing detailed analysis of the diffusion dynamics and brightness (F. Schneider *et al.*, manuscript in preparation).

Analysis of protein partitioning in phase-separated GPMVs

The preference of membrane proteins for the characteristic lipid phases in phase-separated GPMVs was analysed using Fiji/ImageJ as described before [35]. In brief, along a manually defined line connecting regions with ordered and disordered membrane phases on the opposite sides of the vesicle (Fig. S1A), a profile of the protein's intensity was extracted (Fig. S1B). The peak intensity values in the liquid-ordered and liquid-disordered phase (I_{Lo} and I_{Ld}, respectively) were read out and used to calculate the Lo-partitioning percentage (P_{Lo}):

$$P_{Lo} = \frac{100 I_{Lo}}{I_{Lo} + I_{Ld}} \quad (1)$$

For the proteins with frequent partitioning at the border between the two membrane phases, two-colour intensity line profiles along the membrane of each vesicle were manually extracted using FIJI/IMAGEJ (Segmented Line tool with line width of 5 pixels and Spline fit enabled) and further analysed with custom scripts written in Wolfram Mathematica (Champaign, IL, USA). The profiles were first denoised using a Wiener filter, pertaining the peak features. Proteins and lipid-phase boundaries were identified in the green channel (protein) and gradient-filtered red channel (Atto647N-PE), respectively, using the PeakDetect function. For each identified border (170–300 borders from 50–70 intensity profiles per sample), the distance to the closest protein was recorded (d_{min}, as indicated in Fig. 1C and exemplified in Fig. S3C). For all borders from each sample, the cumulative distribution function of minimal border-to-protein distances was calculated ($CDF(d_{min})$, Fig. S3D), and compared with those generated from the same profiles with the two channels slid with respect to each other for a random spatial shift ($CDF_{rand}(d_{min})$):

$$\text{Cumulative enrichment}: CE(d_{min}) = \frac{CDF(d_{min})}{CDF_{rand}(d_{min})} \quad (2)$$

Figures 1C and 2D display the averages and standard deviations of the Cumulative enrichment factor (CE) calculated for 200 randomly shifted profiles per analysed image; values above 1 thus indicate above-random occurrences of d_{min}.

To statistically assess the probability that the observed enrichment at low d_{min} was caused by random chance, we compared two hypothetical models: a random ($CE_{random} = 1$) and the simplest border-enriched distribution ($CE_{border} = 1 + a \exp(-d_{min}/d_0)$). In determining the fitted parameters of the latter, the experimental uncertainties of individual data points (σ_i) were taken into account by weighting their contribution with factors of $1/\sigma_i^2$. For each model (CE_j, j = border, random), the weighted sum of the squared residuals ($WSSR$) was calculated over all n data points i of an experimental dataset (CE_{exp}):

$$WSSR_j = \sigma^2 \sum_{i=1}^{n} \frac{\left(CE_{exp,i} - CE_{j,i}\right)^2}{\sigma_i^2}, \ \sigma^{-2} = \sum_{i=1}^{n} \sigma_i^{-2} \quad (3)$$

These residuals were further used to calculate the Bayesian Information Criterion of each model (BIC_j):

$$BIC_j = n \ln\left(\frac{WSSR_j}{n}\right) + k_j \ln(n), \quad (4)$$

which also penalises each model for the number of its adjustable parameters k_j ($k_{border} = 2$, $k_{random} = 0$).

Finally, the relative likelihood value for the random distribution relative to the border-enriched model (RL_{random}) was calculated [82]:

$$RL_{random} = \exp\left(\frac{BIC_{border} - BIC_{random}}{2}\right). \quad (5)$$

The low values of RL_{random} displayed in Figs 1C and 2D thus indicate that the measured data unlikely arose from a random distribution with no border enrichment. As the negative control, we calculated the RL_{random} values also for the randomly shifted profiles; for the three datasets presented in Figs 1C and Fig. 2D, the medians of RL_{random} ranged between 7 and 9, indicating that the scrambled data are indeed better described by the random distribution than by a border-enriched model.

For TCR aggregates in GPMVs derived from activated Jurkat cells (Figs 2A, S4A) and CHO cells (Fig. S4D), the quantification yielded high RL_{random} values signifying no overall border enrichment. We believe this was due to the remaining nonclustered signal of the protein after incomplete aggregation – OKT3 alone was used to activate the T cells, while CHO cells showed a very high expression level of the TCR. The remaining nonclustered signal was (a) less likely to localise at the border, and (b) more likely to contribute border localisations in the randomised reference data, used in the calculation of the Cumulative border enrichment and thereby RL_{random}.

Spectral imaging of GPMVs and live cells

To monitor membrane order in GPMVs, these were incubated with the polarity-sensitive membrane dye NR12S [47] at a concentration of 0.05 µg/ml for 30 min. Homogeneous vesicles were imaged at room temperature in plastic-bottom 8-well microscopy chambers (ibidi µslides), whereas for phase separation at 4 °C, Vaseline-sealed observation chambers were used, as described above.

To measure membrane order in live cells with respect to a protein's location, cells were first incubated in HBS with the corresponding Fabs: plain Jurkats with anti-CD3 or anti-CD45 Fabs labelled with Alexa Fluor 488 at 0.2 µg·mL^{-1} on ice, Jurkat TCR-mNG with 50 ng·µL^{-1} of UCHT-1CD45RO-C-tag/His-tag Fab in RPMI without supplements at 37 °C. After 15 min, NR12S was added (0.5 µg·mL^{-1}), and cells were left to incubate for another 5 min before washing with warm HBS. Cells were then carefully dropped onto the surface of interest (antibody-coated coverslip or protein-decorated SLB) on the microscope stage (37 °C and 5% CO_2) and left for 5–10 min to settle and spread before imaging.

Spectral imaging was conducted using the same microscope as above (or a newer model Zeiss LSM880 with equivalent functionality). Z-stacks of GPMVs were taken with a 40x/1.1 water-immersion objective, as described

above, whereas the bottom membranes of live cells were imaged with a 63x/1.4 oil-immersion objective with spatial sampling around 90 nm/pixel. Fluorescence was excited at 488 nm and detected in the so-called 'Lambda Mode' with 22 channels within the spectral range 500–695 nm, that is with a wavelength step of 8.9 nm.

Analysis of spectral shifts in GPMVs and live cells

To decompose the spectrum $I(\lambda)$ in every pixel of the image into the contributions from the protein (eGFP, mNG, or antibody with Alexa Fluor 488) and the polarity-sensitive membrane probe NR12S, both excited with the 488-nm laser, spectral fitting-based [49] linear unmixing was employed using custom software written in Mathematica (available upon request). Each spectral line-shape was approximated with a transformed log-normal distribution [49], described by three parameters: spectral peak position (λ_{MAX}), full-width at half-maximum (w), and asymmetry (a): $S(\lambda|\lambda_{MAX},w,a)$. Except from λ_{MAX} of NR12S and the relative intensity fraction of the protein spectrum (p), all other spectral parameters were fixed to values optimised on measurements with individual fluorophore to ensure convergence of the unmixing algorithm:

$$I(\lambda) = I_0 \left[pS_{protein}(\lambda) + (1-p)S_{NR12S}(\lambda|\lambda_{MAX}) \right] \quad (6)$$

Here, I_0 denotes the overall intensity, determined by minimisation of least squares [49]. Prior to fitting, the spectra of 3×3 neighbouring pixels were moving-averaged to improve the signal-to-noise ratio and thereby increase spectral sensitivity, and background spectrum from a close-by region subtracted.

To determine the spectral shifts of NR12S at protein aggregates in GPMVs (Figs 3 and S6), aggregates were identified by intensity thresholding, and average peak position of NR12S within the masked region ($\lambda_{MAX,at\ protein}$) compared with membrane parts without protein aggregates ($\lambda_{MAX,elsewhere}$):

$$\text{Spectral shift} = \lambda_{MAX,at\ protein} - \lambda_{MAX,elsewhere} \quad (7)$$

In live cells (Figs 4 and 5), due to less pronounced protein aggregates and higher variations of the NR12S intensity, pixels were classified into groups with high and low local protein concentration based on the relative intensity of the protein signal (p), with thresholding at the median value within each cell. Only central regions of the cells (i.e. with only the bottom membrane in the focus) were analysed. Pixels with a low portion of the membrane signal, where determination of λ_{MAX} was potentially influenced by mis-fitting of the tails of the protein spectrum, were also deemed unreliable and therefore discarded.

As the observed average spectral shifts were small, it was important to ensure they did not arise form interactions

between the dyes or unreliable unmixing. Firstly, note that NR12S localises inside the membrane core while the fluorescent tags of the proteins are outside the membrane, which is usually an unlikely scenario for FRET. Moreover, the potential FRET from the 488-labelled protein to NR12S cannot influence its spectral shifts, as the emission-shifting solvatochromic relaxation occurs only after excitation or energy transfer. In contrast, labelling proteins with a far-red dye, which could accept energy from excited NR12S molecules, would be more prone to FRET-induced artefacts (provided favourable proximity and orientation).

Though FRET was unlikely to bias our data, the unmixing itself could be affected by the contribution from 488-labelled proteins if their spectrum was mis-fitted. However, the different spectral responses for different proteins labelled with the same dye (Fig. 4B, TCR and CD45 labelled with Alexa Fluor 488-tagged Fabs) already indicated that any analysis-induced systematic bias was unlikely. To explicitly assess the robustness of the unmixing, we analysed the aforementioned spectral shifts of NR12S at the protein sites in relation to the relative fraction of the protein signal (p, Fig. S8). The absence of any consistent correlation within all samples corroborates that the claimed effects did not arise from unmixing/FRET artefacts.

To ensure comparability and avoid bias, the routines were fully automatized and repeated with the same set of parameters across all comparable samples. Statistical analysis was performed with PRISM (GraphPad Software, San Diego, CA, USA), as described in each figure caption.

Diffusion measurements of proteins in live cells

The diffusion coefficient of TCR-mNG in the bottom membrane of Jurkat T cells spreading on SLBs (prepared as for spectral imaging) was measured by fluorescence correlation spectroscopy (FCS) using a customised setup [83] built around a RESOLFT microscope (Abberior Instruments), controlled *via* Imspector software, and equipped with a 100x/1.4 oil immersion objective (Olympus) and a stage-top incubator (Okolab) set to 37 °C. The sample was excited with a 488-nm diode laser (PicoQuant) pulsing at 80 MHz and average power 2 μW, measured at the back aperture of the objective, and fluorescence collected by an avalanche photodiode (APD, Excelitas) within the spectral window of 510–565 nm. The signal from the detector was correlated with a hardware correlator (correlator.com Flex02-08D) with typical acquisition times of 10–15 s. Acquisition sites were manually chosen in membrane areas with high protein density. Typically, 2–4 measurements per cell were conducted, each at a different site.

The obtained FCS curves were analysed with FoCuS-point fitting software [84] (freely available at https://github.com/dwaithe/FCS_point_correlator), using the standard model of anomalous 2D diffusion with two triplet components [85] with their correlation times fixed to 0.1

and 2 ms (Fig. S9). From the extracted transit times (τ_{xy}) and estimated diameter of the effective confocal observation spot ($d = 200$ nm, full-width at half-maximum), the diffusion coefficient (D) was calculated using [86]

$$D = \frac{d^2}{8\ln(2)\tau_{xy}} \qquad (8)$$

For the activating condition (adh+pMHC in Fig. 5C), it was challenging to obtain converging and thus reliable correlation curves, for which reason the number of measured instances is lower.

Colocalisation of proteins in GPMVs

For two-colour colocalisation experiments, GPMVs with antibody-stained protein aggregates (or with Atto647N-PE in the negative control, as above) were imaged in plastic-bottom 8-well microscopy chambers (ibidi μslides) at room temperature, using the same instrumentation and settings as for observations of phase-separated GPMVs, described above. The red fluorescence of transmembrane proteins with mRuby3 was excited at 561 nm and collected within 580–630 nm, in a line-interleaved mode with the green channel.

To quantify the colocalisation of protein aggregates in two-channel images of GPMVs, intensity line profiles along the membrane of each vesicle were manually extracted using Fiji/ImageJ (Segmented Line tool with line width of 5 pixels and Spline fit enabled) and further analysed with custom scripts written in Mathematica. The profiles were first denoised using a Wiener filter, pertaining the peak features. By thresholding the data in the reference channel (e.g. of TCR aggregates) at an intensity value at a predefined factor above the background, a mask was created to extract the average intensities of the other channel (e.g. Lck-eGFP) within and outside of the masked regions ($I_{at\,protein}$ and $I_{elsewhere}$, respectively, see Fig. S10B), used to calculate the *Overlap intensity ratio* (*OIR*):

$$\text{Overlap intensity ratio} = \frac{I_{at\,protein}}{I_{elsewhere}} \qquad (9)$$

To compare this to a random distribution, *OIR* was calculated for the intensity profile of the channel of interest split in 50-pixel sections and randomly reshuffled 1000 times (*RandomOIR*), from which the mean and standard deviation were calculated to yield a *Z score* of the experimental *OIR*:

$$\text{Overlap intensity ratio Z score} = \frac{OIR - \text{Mean}\,(RandomOIR)}{\text{St.dev.}\,(RandomOIR)}$$
$$(10)$$

Hence, positive values of the *OIR Z score* indicate above-random colocalisation of signals in the two channels. Statistical analysis was performed with GraphPad Prism, as described in each figure caption.

Author contributions

IU, ES and CE conceived the study; IU, LS, EJ, WG and ES performed the experiments; AMS, CO'BB, MTV and NA prepared custom cell lines and antibodies; IU, LS, WG and ES analysed the data; AMS and FS invaluably contributed to key discussions; IU wrote the manuscript with input from all authors, especially EJ, AMS, FS, ES, and CE.

Data accessibility

The data that support the findings of this study are available in the figures and supplementary material of this article. Original files and code are available from the corresponding author iztok.urbancic@ijs.si upon reasonable request.

References

1 Simons K and Gerl M (2010) Revitalizing membrane rafts: new tools and insights. *Nat Rev Mol Cell Biol* **11**, 688–699.

2 Sezgin E, Leventai I, Mayor S and Eggeling C (2017) The mystery of membrane organization: composition, regulation and roles of lipid rafts. *Nat Rev Mol Cell Biol* **18**, 361–374.

3 Levental I, Lingwood D, Grzybek M, Coskun Ü and Simons K (2010) Palmitoylation regulates raft affinity for the majority of integral raft proteins. *Proc Natl Acad Sci USA* **107**, 22050–22054.

4 Lorent JH, Diaz-Rohrer B, Lin X, Spring K, Gorfe AA, Levental KR and Levental I (2017) Structural determinants and functional consequences of protein affinity for membrane rafts. *Nat Commun* **8**, 1–10.

5 Corradi V, Sejdiu BI, Mesa-Galloso H, Abdizadeh H, Noskov SY, Marrink SJ and Tieleman DP (2019) Emerging diversity in lipid-protein interactions. *Chem Rev* **119**, 5775–5848.

6 Levental I, Levental KR and Heberle FA (2020) Lipid rafts: controversies resolved, mysteries remain. *Trends Cell Biol* **30**, 341–353.

7 Varshney P, Yadav V and Saini N (2016) Lipid rafts in immune signalling: current progress and future perspective. *Immunology* **149**, 13–24.

8 Dustin ML and Baldari CT (2017) The immune synapse: past, present, and future. *Methods Mol Biol Clifton NJ* **1584**, 1–5.

9 Pettmann J, Santos AM, Dushek O and Davis SJ (2018) Membrane ultrastructure and T cell activation. *Front Immunol* **9**, 2152.

10 Wu W, Shi X and Xu C (2016) Regulation of T cell signalling by membrane lipids. *Nat Rev Immunol* **16**, 690–701.

11 Davis SJ and van der Merwe PA (2006) The kinetic-segregation model: TCR triggering and beyond. *Nat Immunol* **7**, 803.

12 Minguet S, Swamy M, Alarcón B, Luescher IF and Schamel WWA (2007) Full activation of the T cell receptor requires both clustering and conformational changes at CD3. *Immunity* **26**, 43–54.

13 Xu C, Gagnon E, Call ME, Schnell JR, Schwieters CD, Carman CV, Chou JJ and Wucherpfennig KW (2008) Regulation of T cell receptor activation by dynamic membrane binding of the CD3epsilon cytoplasmic tyrosine-based motif. *Cell* **135**, 702–713.

14 Swamy M, Beck-Garcia K, Beck-Garcia E, Hartl FA, Morath A, Yousefi OS, Dopfer EP, Molnár E, Schulze AK, Blanco R *et al.* (2016) A cholesterol-based allostery model of T cell receptor phosphorylation. *Immunity* **44**, 1091–1101.

15 Xavier R, Brennan T, Li Q, McCormack C and Seed B (1998) Membrane compartmentation is required for efficient T cell activation. *Immunity* **8**, 723–732.

16 Viola A, Schroeder S, Sakakibara Y and Lanzavecchia A (1999) T lymphocyte costimulation mediated by reorganization of membrane microdomains. *Science* **283**, 680–682.

17 Montixi C, Langlet C, Bernard AM, Thimonier J, Dubois C, Wurbel MA, Chauvin JP, Pierres M and He HT (1998) Engagement of T cell receptor triggers its recruitment to low-density detergent-insoluble membrane domains. *EMBO J* **17**, 5334–5348.

18 Giurisato E, McIntosh DP, Tassi M, Gamberucci A and Benedetti A (2003) T cell receptor can be recruited to a subset of plasma membrane rafts, independently of cell signaling and attendantly to raft clustering. *J Biol Chem* **278**, 6771–6778.

19 Drevot P, Langlet C, Guo X-J, Bernard A-M, Colard O, Chauvin J-P, Lasserre R and He H-T (2002) TCR signal initiation machinery is pre-assembled and activated in a subset of membrane rafts. *EMBO J* **21**, 1899–1908.

20 Janes PW, Ley SC and Magee AI (1999) Aggregation of lipid rafts accompanies signaling via the T cell antigen receptor. *J Cell Biol* **147**, 447–461.

21 Gri G, Molon B, Manes S, Pozzan T and Viola A (2004) The inner side of T cell lipid rafts. *Immunol Lett* **94**, 247–252.

22 Dinic J, Riehl A, Adler J and Parmryd I (2015) The T cell receptor resides in ordered plasma membrane nanodomains that aggregate upon patching of the receptor. *Sci Rep* **5**, 10082.

23 Gaus K, Chklovskaia E, de St F, Groth B, Jessup W and Harder T (2005) Condensation of the plasma membrane at the site of T lymphocyte activation. *J Cell Biol* **171**, 121–131.

24 Rentero C, Zech T, Quinn CM, Engelhardt K, Williamson D, Grewal T, Jessup W, Harder T and Gaus K (2008) Functional implications of plasma membrane condensation for T cell activation. *PLoS ONE* **3**, e2262.

25 Owen DM, Oddos S, Kumar S, Davis DM, Neil MAA, French PMW, Dustin ML, Magee AI and Cebecauer M (2010) High plasma membrane lipid order imaged at the immunological synapse periphery in live T cells. *Mol Membr Biol* **27**, 178–189.

26 Hashimoto-Tane A, Yokosuka T, Ishihara C, Sakuma M, Kobayashi W and Saito T (2010) T-cell receptor microclusters critical for T-cell activation are formed independently of lipid raft clustering. *Mol Cell Biol* **30**, 3421–3429.

27 Lillemeier BF, Mörtelmaier MA, Forstner MB, Huppa JB, Groves JT and Davis MM (2010) TCR and Lat are expressed on separate protein islands on T cell membranes and concatenate during activation. *Nat Immunol* **11**, 90–96.

28 Santos AM, Ponjavic A, Fritzsche M, Fernandes RA, Serna JB, Wilcock MJ, Schneider F, Urbančič I, McColl J, Anzilotti C *et al.* (2018) Capturing resting T cells: the perils of PLL. *Nat Immunol* **19**, 203–205.

29 Molnár E, Swamy M, Holzer M, Beck-Garćia K, Worch R, Thiele C, Guigas G, Boye K, Luescher IF,

Schwille P *et al.* (2012) Cholesterol and sphingomyelin drive ligand-independent T-cell antigen receptor nanoclustering. *J Biol Chem* **287**, 42664–42674.

30 Beck-García K, Beck-García E, Bohler S, Zorzin C, Sezgin E, Leventhal I, Alarcón B and Schamel WWA (2015) Nanoclusters of the resting T cell antigen receptor (TCR) localize to non-raft domains. *Biochim Biophys Acta* **1853**, 802–809.

31 Stone MB, Shelby SA, Núñez MF, Wisser K and Veatch SL. (2017) Protein sorting by lipid phase-like domains supports emergent signaling function in B lymphocyte plasma membranes. *eLife* **6**, e19891.

32 Núñez MF, Wisser K and Veatch SL (2020) Synergistic factors control kinase-phosphatase organization in B-cells engaged with supported bilayers. *Mol Biol Cell* **31**, 667–682.

33 Field KA, Holowka D and Baird B (1995) Fc epsilon RI-mediated recruitment of p53/56lyn to detergent-resistant membrane domains accompanies cellular signaling. *Proc Natl Acad Sci USA* **92**, 9201–9205.

34 Felce JH, Sezgin E, Wane M, Brouwer H, Dustin ML, Eggeling C and Davis SJ (2018) CD45 exclusion- and cross-linking-based receptor signaling together broaden FcεRI reactivity. *Sci Signal* **11**, eaat0756.

35 Sezgin E, Kaiser H-J, Baumgart T, Schwille P, Simons K and Leventhal I (2012) Elucidating membrane structure and protein behavior using giant plasma membrane vesicles. *Nat Protoc* **7**, 1042–1051.

36 Baumgart T, Hammond AT, Sengupta P, Hess ST, Holowka DA, Baird BA and Webb WW (2007) Large-scale fluid/fluid phase separation of proteins and lipids in giant plasma membrane vesicles. *Proc Natl Acad Sci USA* **104**, 3165–3170.

37 Honigmann A, Mueller V, Ta H, Schoenle A, Sezgin E, Hell SW and Eggeling C (2014) Scanning STED-FCS reveals spatiotemporal heterogeneity of lipid interaction in the plasma membrane of living cells. *Nat Commun* **5**, 5412.

38 Shenoy-Scaria AM, Gauen LK, Kwong J, Shaw AS and Lublin DM (1993) Palmitylation of an amino-terminal cysteine motif of protein tyrosine kinases p56lck and p59fyn mediates interaction with glycosyl-phosphatidylinositol-anchored proteins. *Mol Cell Biol* **13**, 6385–6392.

39 Kabouridis PS, Magee AI and Ley SC (1997) S-acylation of LCK protein tyrosine kinase is essential for its signalling function in T lymphocytes. *EMBO J* **16**, 4983–4998.

40 Rossy J, Owen DM, Williamson DJ, Yang Z and Gaus K (2013) Conformational states of the kinase Lck regulate clustering in early T cell signaling. *Nat Immunol* **14**, 82–89.

41 Ji Y, Leymarie N, Haeussler DJ, Bachschmid MM, Costello CE and Lin C (2013) Direct detection of S-Palmitoylation by mass spectrometry. *Anal Chem* **85**, 11952–11959.

42 Liang Q, Wu Q-Y and Wang Z-Y (2014) Effect of hydrophobic mismatch on domain formation and peptide sorting in the multicomponent lipid bilayers in the presence of immobilized peptides. *J Chem Phys* **141**, 074702.

43 Yang S-T, Kreutzberger AJB, Kiessling V, Ganser-Pornillos BK, White JM and Tamm LK (2017) HIV virions sense plasma membrane heterogeneity for cell entry. *Sci Adv* **3**, e1700338.

44 Li G, Wang Q, Kakuda S and London E (2020) Nanodomains can persist at physiologic temperature in plasma membrane vesicles and be modulated by altering cell lipids. *J Lipid Res* **61**, 758–766.

45 Kaiser H-J, Lingwood D, Leventhal I, Sampaio JL, Kalvodova L, Rajendran L and Simons K (2009) Order of lipid phases in model and plasma membranes. *Proc Natl Acad Sci USA* **106**, 16645.

46 Zhou Y, Maxwell KN, Sezgin E, Lu M, Liang H, Hancock JF, Dial EJ, Lichtenberger LM and Leventhal I (2013) Bile acids modulate signaling by functional perturbation of plasma membrane domains. *J Biol Chem* **288**, 35660–35670.

47 Kucherak OA, Oncul S, Darwich Z, Yushchenko DA, Arntz Y, Didier P, Mély Y and Klymchenko AS (2010) Switchable nile red-based probe for cholesterol and lipid order at the outer leaflet of biomembranes. *J Am Chem Soc* **132**, 4907–4916.

48 Sezgin E, Schneider F, Zilles V, Urbančič I, Garcia E, Waithe D, Klymchenko AS and Eggeling C (2017) Polarity-sensitive probes for superresolution stimulated emission depletion microscopy. *Biophys J* **113**, 1321–1330.

49 Urbančič I, Arsov Z, Ljubetič A, Biglino D and Štrancar J (2013) Bleaching-corrected fluorescence microspectroscopy with nanometer peak position resolution. *Opt Express* **21**, 25291–25306.

50 Dinic J, Ashrafzadeh P and Parmryd I (2013) Actin filaments attachment at the plasma membrane in live cells cause the formation of ordered lipid domains. *Biochim Biophys Acta* **1828**, 1102–1111.

51 Schneider F, Waithe D, Clausen MP, Galiani S, Koller T, Ozhan G, Eggeling C and Sezgin E (2017) Diffusion of lipids and GPI-anchored proteins in actin-free plasma membrane vesicles measured by STED-FCS. *Mol Biol Cell* **28**, 1507–1518.

52 Sasmal DK, Feng W, Roy S, Leung P, He Y, Cai C, Cao G, Lian H, Qin J, Hui E *et al.* (2020) TCR–pMHC bond conformation controls TCR ligand discrimination. *Cell Mol Immunol* **17**, 203–217.

53 Jenkins E, Santos AM, O'Brien-Ball C, Felce JH, Wilcock MJ, Hatherley D, Dustin ML, Davis SJ, Eggeling C and Sezgin E (2018) Reconstitution of

immune cell interactions in free-standing membranes. *J Cell Sci* **132**, jcs219709.

54 Ma Y, Lim YJ, Benda A, Lou J, Goyette J and Gaus K (2020) Clustering of the ζ-Chain can initiate T cell receptor signaling. *Int J Mol Sci* **21**, 3498.

55 Goose JE and Sansom MSP (2013) Reduced lateral mobility of lipids and proteins in crowded membranes. *PLoS Comput Biol* **9**, e1003033.

56 Briones R, Aponte-Santamaría C and de Groot BL (2017) Localization and ordering of lipids around aquaporin-0: protein and lipid mobility effects. *Front Physiol* **8**, 124.

57 Frese RN, Pàmies JC, Olsen JD, Bahatyrova S, van der Weij-de Wit CD, Aartsma TJ, Otto C, Hunter CN, Frenkel D and van Grondelle R (2008) Protein shape and crowding drive domain formation and curvature in biological membranes. *Biophys J* **94**, 640–647.

58 Tulodziecka K, Diaz-Rohrer BB, Farley MM, Chan RB, Di Paolo G, Leventual KR, Waxham MN and Leventual I (2016) Remodeling of the postsynaptic plasma membrane during neural development. *Mol Biol Cell* **27**, 3480–3489.

59 Dietrich C, Volovyk ZN, Levi M, Thompson NL and Jacobson K (2001) Partitioning of Thy-1, GM1, and cross-linked phospholipid analogs into lipid rafts reconstituted in supported model membrane monolayers. *Proc Natl Acad Sci USA* **98**, 10642–10647.

60 Hammond AT, Heberle FA, Baumgart T, Holowka D, Baird B and Feigenson GW (2005) Crosslinking a lipid raft component triggers liquid ordered-liquid disordered phase separation in model plasma membranes. *Proc Natl Acad Sci USA* **102**, 6320–6325.

61 Raghupathy R, Anilkumar AA, Polley A, Singh PP, Yadav M, Johnson C, Suryawanshi S, Saikam V, Sawant SD, Panda A *et al.* (2015) Transbilayer lipid interactions mediate nanoclustering of lipid-anchored proteins. *Cell* **161**, 581–594.

62 Fujimoto T and Parmryd I (2017) Interleaflet coupling, pinning, and leaflet asymmetry—major players in plasma membrane nanodomain formation. *Front Cell Dev Biol* **4**, 155.

63 Kinoshita M, Suzuki KGN, Matsumori N, Takada M, Ano H, Morigaki K, Abe M, Makino A, Kobayashi T, Hirosawa KM *et al.* (2017) Raft-based sphingomyelin interactions revealed by new fluorescent sphingomyelin analogs. *J Cell Biol* **216**, 1183–1204.

64 Risselada HJ and Marrink SJ (2008) The molecular face of lipid rafts in model membranes. *Proc Natl Acad Sci USA* **105**, 17367–17372.

65 Amzel LM (1997) Loss of translational entropy in binding, folding, and catalysis. *Proteins* **28**, 144–149.

66 Urbančič I, Ljubetič A and Štrancar J (2014) Resolving internal motional correlations to complete the conformational entropy meter. *J Phys Chem Lett* **5**, 3593–3600.

67 Baron R, de Vries AH, Hünenberger PH and van Gunsteren WF (2006) Configurational entropies of lipids in pure and mixed bilayers from atomic-level and coarse-grained molecular dynamics simulations. *J Phys Chem B* **110**, 15602–15614.

68 Gesper A, Wennmalm S, Hagemann P, Eriksson S-G, Happel P and Parmryd I. (2020) Variations in plasma membrane topography can explain heterogenous diffusion coefficients obtained by fluorescence correlation spectroscopy. *Front Cell Develop Biol* **8**, 767.

69 Fernandes RA, Ganzinger KA, Tzou JC, Jönsson P, Lee SF, Palayret M, Santos AM, Carr AR, Ponjavic A, Chang VT *et al.* (2019) A cell topography-based mechanism for ligand discrimination by the T cell receptor. *Proc Natl Acad Sci USA* **116**, 14002–14010.

70 Miguel L, Owen DM, Lim C, Liebig C and Evans J (1950) Magee AI & Jury EC (2011) Primary human CD4+ T cells have diverse levels of membrane lipid order that correlate with their function. *J Immunol Baltim Md* **186**, 3505–3516.

71 Gaus K, Le Lay S, Balasubramanian N and Schwartz MA (2006) Integrin-mediated adhesion regulates membrane order. *J Cell Biol* **174**, 725–734.

72 Honigmann A, Sadeghi S, Keller J, Hell SW, Eggeling C and Vink R (2014) A lipid bound actin meshwork organizes liquid phase separation in model membranes. *eLife* **3**, e01671.

73 Fawcett VCJ and Lorenz U (1950) (2005) Localization of Src homology 2 domain-containing phosphatase 1 (SHP-1) to lipid rafts in T lymphocytes: functional implications and a role for the SHP-1 carboxyl terminus. *J Immunol* **174**, 2849–2859.

74 Coelho S, Baek J, Graus MS, Halstead JM, Nicovich PR, Feher K, Gandhi H, Gooding JJ and Gaus K (2020) Ultraprecise single-molecule localization microscopy enables in situ distance measurements in intact cells. *Sci Adv* **6**, eaay8271.

75 Schneider F, Colin-York H and Fritzsche M (2021) Quantitative bio-imaging tools to dissect the interplay of membrane and cytoskeletal actin dynamics in immune cells. *Front Immunol* **11**, 612542.

76 Hellmeier J, Platzer R, Eklund AS, Schlichthaerle T, Karner A, Motsch V, Schneider MC, Kurz E, Bamieh V, Brameshuber M *et al.* (2021) DNA origami demonstrate the unique stimulatory power of single pMHCs as T cell antigens. *Proc Natl Acad Sci USA* **118**.

77 Chang VT, Fernandes RA, Ganzinger KA, Lee SF, Siebold C, McColl J, Jönsson P, Palayret M, Harlos K, Coles CH *et al.* (2016) Initiation of T cell signaling by CD45 segregation at "close contacts". *Nat Immunol* **17**, 574–582.

78 Arnett KL, Harrison SC and Wiley DC (2004) Crystal structure of a human CD3-epsilon/delta dimer in

complex with a UCHT1 single-chain antibody fragment. *Proc Natl Acad Sci USA* **101**, 16268–16273.

79 Altman JD, Moss PA, Goulder PJ, Barouch DH, McHeyzer-Williams MG, Bell JI, McMichael AJ and Davis MM (1996) Phenotypic analysis of antigen-specific T lymphocytes. *Science* **274**, 94–96.

80 Hardy GJ, Nayak R and Zauscher S (2013) Model cell membranes: Techniques to form complex biomimetic supported lipid bilayers via vesicle fusion. *Curr Opin Colloid Interface Sci* **18**, 448–458.

81 Khan F, He M and Taussig MJ (2006) Double-hexahistidine tag with high-affinity binding for protein immobilization, purification, and detection on ni-nitrilotriacetic acid surfaces. *Anal Chem* **78**, 3072–3079.

82 Lagerholm BC, Andrade DM, Clausen MP and Eggeling C (2017) Convergence of lateral dynamic measurements in the plasma membrane of live cells from single particle tracking and STED-FCS. *J Phys D* **50**, 063001.

83 Galiani S, Waithe D, Reglinski K, Cruz-Zaragoza LD, Garcia E, Clausen MP, Schliebs W, Erdmann R and Eggeling C (2016) Super-resolution microscopy reveals compartmentalization of peroxisomal membrane proteins. *J Biol Chem* **291**, 16948–16962.

84 Waithe D, Clausen MP, Sezgin E and Eggeling C (2016) FoCuS-point: software for STED fluorescence correlation and time-gated single photon counting. *Bioinforma* **32**, 958–960.

85 Steiert F, Petrov EP, Schultz P, Schwille P and Weidemann T (2018) Photophysical behavior of mNeonGreen, an evolutionarily distant green fluorescent protein. *Biophys J* **114**, 2419–2431.

86 Sezgin E, Schneider F, Galiani S, Urbančič I, Waithe D, Lagerholm BC and Eggeling C (2019) Measuring nanoscale diffusion dynamics in cellular membranes with super-resolution STED–FCS. *Nat Protoc* **14**, 1054.

Supporting information

Additional supporting information may be found online in the Supporting Information section at the end of the article.

Fig. S1. Determination of proteins' Lo partitioning percentage.

Fig. S2. Lo partitioning percentages for transmembrane (tm-) protein domains and their membrane-anchor mutants in GPMVs.

Fig. S3. Partitioning of fluorescent Lck constructs in GPMVs.

Fig. S4. Partitioning of protein aggregates in phase-separated GPMVs.

Fig. S5. Protein crosslinking with primary antibodies.

Fig. S6. Determination of membrane order in GPMVs with proteins clustered by antibodies.

Fig. S7. Membrane order in phase-separated GPMVs.

Fig. S8. Evaluation of spectral unmixing.

Fig. S9. Exemplary FCS curves of TCR-mNeonGreen in Jurkat T cells spreading on SLBs.

Fig. S10. Colocalisation of proteins in GPMVs - controls and analysis.

Fig. S11. Colocalisation of transmembrane protein constructs with Lck in GPMVs.